4-2024

Does El Niño affect MJO-AR connections over the North Pacific and associated North American precipitation?

Laís G. Fernandes
Portland State University

Paul Loikith
Portland State University, ploikith@pdx.edu

Citation Details

Fernandes, L.G., Loikith, P.C. Does El Niño affect MJO-AR connections over the North Pacific and associated North American precipitation?. Clim Dyn (2024). https://doi-org.proxy.lib.pdx.edu/10.1007/s00382-024-07177-3

Does El Niño affect MJO-AR connections over the North Pacific and associated North American precipitation?

Laís Gonçalves Fernandes
lais.fernandes@pdx.edu
Portland State University https://orcid.org/0000-0001-7228-6464
Paul C. Loikith
Portland State University

Research Article

Keywords: EN-MJO Interaction, MJO-AR connections, North Pacific ARs, AR landfall precipitation, extreme AR precipitation events

Posted Date: August 3rd, 2023

DOI: https://doi.org/10.21203/rs.3.rs-3171430/v1

Version of Record: A version of this preprint was published at Climate Dynamics on March 22nd, 2024. See the published version at https://doi.org/10.1007/s00382-024-07177-3.

Does El Niño affect MJO-AR connections over the North Pacific and associated North American precipitation?

Laís G. Fernandes [1*] and Paul C. Loikith [1]

[1] Department of Geography, Portland State University, Portland, OR, United States

Laís G. Fernandes ORCID ID: https://orcid.org/0000-0001-7228-6464
Paul C. Loikith ORCID ID: https://orcid.org/0000-0002-2352-0565

*Corresponding author address: Department of Geography, PSU, 1825 SW Broadway Portland, OR 97201. E-mail: lais.fernandes@pdx.edu

Does El Niño affect MJO-AR connections over the North Pacific and associated North American precipitation?

Laís G. Fernandes [1*], and Paul C. Loikith [1]

[1] Department of Geography, Portland State University, Portland, OR, United States

Abstract

This study investigates how the positive phase of the El Niño-Southern Oscillation (EN) influences the Madden-Julian Oscillation (MJO) modulation of cool-season North Pacific atmospheric rivers (ARs) and associated AR-landfall driven precipitation over North America. EN changes the key drivers of MJO-AR connections by shifting MJO-driven convection east of 180° longitude in MJO phases 6-8 and extending the northern Pacific subtropical jet eastward. Under these conditions, the MJO tropical-extratropical teleconnection is triggered east of 180° in MJO phases 7-8, and a persistent cyclonic flow anomaly develops along the United States west coast. Anomalous northeastward integrated water vapor transport (IVT) within the cyclonic flow coupled with the MJO convection over the western (phase 7) and central (phase 8) Pacific increases AR frequency, shifting it to the east over regions that do not show a relationship with EN or MJO alone. Besides enhancing AR activity, EN background conditions increase the number of AR events, their lifetime, and mean intensity from MJO phases 6 through 8, as well as the number of MJO active days, AR initiations, and ARs making landfall over North America in MJO phases 8-1. The positive precipitation anomalies and increased frequency of extreme precipitation events associated with landfalling North Pacific ARs related to MJO are also shifted to the east in EN, enhancing and extending rainfall over western North America in MJO phases 6-1. Results provide new insight into the drivers of AR activity and associated precipitation along the west coast of North America with implications for improving subseasonal-to-seasonal predictions.

Keywords: EN-MJO Interaction, MJO-AR connections, North Pacific ARs, AR landfall precipitation, extreme AR precipitation events.

[*] *Corresponding author address*: Department of Geography, PSU, 1825 SW Broadway Portland, OR 97201. E-mail: lais.fernandes@pdx.edu

1 Introduction

Atmospheric rivers (ARs), long and narrow channels of enhanced water vapor transport in the lower troposphere, are responsible for over 90% of the water vapor transported between the tropics and extratropics (Zhu and Newell 1994, 1998). They are the primary driver of extreme precipitation and hydrological events during the cool-season in western North America while also being critical for water supply (Ralph et al. 2006; Neiman et al. 2008a, b; Leung and Qian 2009; Dettinger et al. 2011; Neiman et al. 2011; Warner, Mass and Salatheé 2012; Toride et al. 2019).

New algorithms to track the lifecycle of ARs (Sellars et al. 2017; Zhou, Kim and Guan 2018; Guan and Waliser 2019; Shearer et al. 2020) have helped improve their prediction, including their likely propagation, termination location, and hydrological impacts. However, the consistency of lifecycle tracking methods in representing the modulation of ARs by natural climate variability modes, such as the El Niño-Southern Oscillation (ENSO) and the Madden-Julian Oscillation (MJO), is the subject of ongoing investigation (Zhou et al. 2021). Previous research has shown that landfalling ARs in western North America are more frequent when MJO convection is active over the western Pacific (Guan et al. 2012, 2013; Payne and Magnusdottir 2014; Spry et al. 2014). The new tracking algorithms may help to improve the prediction of landfalling ARs on subseasonal time scales (2-5 weeks) through the assessment of MJO-AR connections (Baggett et al. 2017; Mundhenk et al. 2018; DeFlorio et al. 2018, 2019) as the MJO drives the North Pacific AR activity on subseasonal time scales (Mundhenk, Barnes and Maloney 2016).

Recently, Zhou, Kim and Waliser (2021) and Zhou et al. (2021), using the lifecycle tracking method of Zhou, Kim and Guan (2018), demonstrated that MJO modulates North Pacific AR lifecycles in the cool-season (November-March, NDJFM). The most significant impacts happen in phases 2+3 and 6+7, with changes in the number of AR events, their lifetime, intensity, frequency and their origins over the subtropical Pacific. Moreover, Zhou et al. (2021) found consistent ENSO-AR and MJO-AR connections over the North Pacific among global AR detection algorithms.

Previous investigations have described the ENSO modulation of AR activity over the North Pacific (Payne and Magnusdottir 2014; Guan and Waliser 2015; Mundhenk, Barnes and Maloney 2016; Kim, Zhou and Alexander 2017; Patricola et al. 2020). El Niño (EN) increases AR activity over the northeastern Pacific and the northwest coast of the US (Guan and Waliser 2015; Mundhenk Barnes, and Maloney 2016; Kim, Zhou and Alexander 2017; Patricola et al. 2020). Zhou et al. (2021) found that both active ENSO states (EN and La Niña, LN) increase AR frequency over the west coast of North America around 30°N.

The MJO modulation of North Pacific ARs and their lifecycles may change when ENSO is in the positive (EN) or negative (LN) phase, complicating subseasonal predictions. The active ENSO states modify the background through which both ARs (subtropical North Pacific) and MJO (tropical Pacific) propagate. Also, EN shifts the MJO activity eastward into the central Pacific, expanding the longitudinal domain of its convective activity and decreasing propagation speed (Fink and Speth 1997; Hendon, Zhang and Glick 1999; Kessler 2001; Tam and Lau 2005; Wei and Ren 2019). Changes in the MJO structure and propagation under EN (phases 6-1) happen when the MJO modulates North Pacific ARs (phases 6+7, Zhou, Kim and Waliser 2021; Zhou et al. 2021).

Other studies have focused on the ENSO-driven modulation of MJO tropical-extratropical teleconnections over the North Pacific (Roundy et al. 2010; Moon, Wang and Ha 2011; Arcodia, Kirtman and Siqueira 2020; Tseng, Maloney and Barnes 2020). Moon, Wang and Ha (2011) have shown that in MJO phase 7, the North Pacific cyclonic flow strengthens, and is closer to the western US in EN, increasing precipitation over that region. Also, the combined effects of EN and MJO phases 6+7 produce significant variability in southeastern US rainfall (Arcodia, Kirtman and Siqueira 2020). Conversely, Tseng, Maloney and Barnes (2020) found that the influence of MJO tropical-extratropical teleconnections in the extratropics reduces in EN. The southeastward extension of the northern Pacific subtropical jet in EN decreases the Rossby wave propagation reducing the MJO teleconnection pattern consistency. Changes in the MJO teleconnections by ENSO may impact the lifecycles of North Pacific ARs.

Previous results showing nonlinear interactions between ENSO and MJO over the North Pacific and North America (Roundy et al. 2010; Arcodia, Kirtman and Siqueira 2020) highlight the importance of investigating how both modes influence North Pacific ARs simultaneously. For example, Mundhenk, Barnes and Maloney (2016) pointed out a complex interaction between ENSO and MJO over the northeastern Pacific impacting ARs. The combined use of AR frequency and circulation composites based solely on the MJO and ENSO separately might not be enough to effectively describe the associated AR weather patterns when both modes are active.

Recently, Toride and Hakim (2021) pointed out that EN favors northern Pacific AR activity in MJO phase 3 because it weakens the North Pacific anticyclonic flow. However, changes in the circulation by EN in other MJO phases have not been described, such as in phases 6+7 when the origin of ARs over the subtropical northern Pacific increases (Zhou, Kim and Waliser 2021; Zhou et al. 2021). Furthermore, ENSO variability affects the strength and position of the northern Pacific subtropical jet (Bjerknes 1969), one of the key drivers of the MJO-AR connections. Changes in the subtropical jet are crucial as they impact the MJO tropical-extratropical teleconnection more than MJO heating, fixing the teleconnection route (Bao and Hartmann 2014).

Here we aim to assess how EN influences the MJO modulation of cool-season North Pacific AR lifecycle characteristics and associated precipitation over North America. EN may affect MJO-AR connections through changes in the basic state and in the MJO forcing. We address the following questions: (1) Does EN affect the MJO modulation of North Pacific ARs? (2) How does EN change the key drivers of the MJO-AR connections? (3) Does the overlapping effect of EN and MJO contribute to landfalling North Pacific ARs, their precipitation, and extremes over western North America? The proposed assessment is crucial to subseasonal predictions because both ENSO and MJO are known as "windows of opportunity" for extended subseasonal predictability (Vitart et al. 2015).

The data and methodology are described in Section 2. In Section 3, we examine the ENSO modulation of North Pacific ARs and the MJO modulation of North Pacific ARs. The EN influence on MJO-AR connections over North Pacific and North America is shown in Section 4. Section 5 describes the EN influence on MJO-AR precipitation anomalies and extreme precipitation events over North America. The results are summarized and discussed in Section 6.

2 Data and Methodology

2.1 Data

Daily vertically integrated water vapor transport (IVT), 300 hPa wind, and bias-corrected precipitation data are from the Modern-Era Retrospective Analysis for Research and Applications, version 2 (MERRA-2, Gelaro et al. 2017), provided on a 0.5° latitude by 0.675° longitude grid. Daily data from CPC rainfall (Chen et al. 2008), gridded to 0.5°, are used for comparisons with precipitation data from MERRA-2. Daily outgoing longwave radiation (OLR) on a 2.5° latitude/longitude grid are from Liebmann and Smith (1996). The analysis period is 1980-2020 over the cool-season (NDJFM), when ENSO and MJO are more mature (Moon, Wang and Ha 2011) and ARs are more active over the North Pacific (Guan and Waliser 2015; Mundhenk, Barnes and Maloney 2016; Stan et al. 2017) and in western North America (Slinskey et al. 2020).

2.2 Methodology

2.2.1 AR events

Only AR events that originate between 0°N-60°N and 100°E-100°W (dashed rectangle in Fig. 1a) as provided by the Guan and Waliser (2019) AR detection/tracking algorithm are included in the analysis. ARs are detected every six hours using the MERRA-2 based dataset of Guan and Waliser (2019). We follow Zhou et al. (2021) and consider the term "detection" in association with AR objects and "tracking" for tracing ARs' lifecycles. While there are other available AR detection and tracking algorithms, and the choice of algorithm will necessarily affect results to some degree, we choose Guan and Waliser's (2019) approach in part because it handles AR separation/merges well, thus contributing to a higher detection/tracking sensitivity than previous algorithms (Sellars et al. 2017; Zhou, Kim and Guan 2018). Its efficacy is also well established and used in many published studies (Bozkurt et al. 2021; Chakraborty et al. 2021; Kim and Chiang 2021; Prince et al. 2021; Lee, Polvani and Guan 2022; Nash et al. 2022; Guan, Waliser and Ralph 2023). Additional information regarding the algorithm and its evaluation can be found in Guan and Waliser (2019).

An AR object is an enclosed 2-dimensional (latitude and longitude) spatially contiguous area of anomalously strong IVT that meets the criteria for AR conditions including IVT magnitude and geometric constraints on length and width. Objects first retained from IVT magnitude thresholding (above the 85th percentile) are filtered using directional and geometric requirements. First, more than 50% of the area of the IVT object must have an IVT direction within 45° of the mean IVT direction of the object. This ensures general coherence in IVT direction within the object. Secondly, only objects longer than 2000 km with length-to-width ratios >2 are retained. Finally, multiple, sequentially higher IVT thresholds (85th-95th percentiles) are applied if an IVT object fails the previous criteria. The use of multiple IVT thresholds allows for the identification of ARs within the core region of a larger, wider object that may not meet the geometry criteria (Guan, Waliser and Ralph 2018). Objects that are retained after these steps are labeled ARs.

Each AR event is a set of spatiotemporally connected AR objects, with the first object defined as the AR origin (Fig. 1a) (Zhou, Kim and Guan 2018; Guan and Waliser 2019). For instance, Fig. 1a shows an example of an AR event across its entire lifecycle concurrent with EN and MJO phases 7-1 during November 16-22, 1982, lasting 24 six-hourly time steps. The AR event originated in MJO phase 7 on November 16, propagated over North America under MJO phase 8 during November 17-21, and ended on November 22 when MJO was in phase 1. We calculate the AR frequency as the grid-point-accumulated number of AR objects from one lifecycle divided by the number of time steps (Zhou, Kim and Waliser 2021; Zhou et al. 2021). Hence, the AR frequency here shows the extent of an area affected by an AR event (Fig. 1b). For example, within the 24 six-hourly time steps of the AR event in Figure 1b, some grid points over Mexico are impacted by this AR for 45% of the lifetime (about 10-11 time steps, Fig. 1c). The winter climatology (NDJFM) AR frequency is computed similarly except considering all six-hourly time steps during 40 winters, and all ARs originated within our study domain.

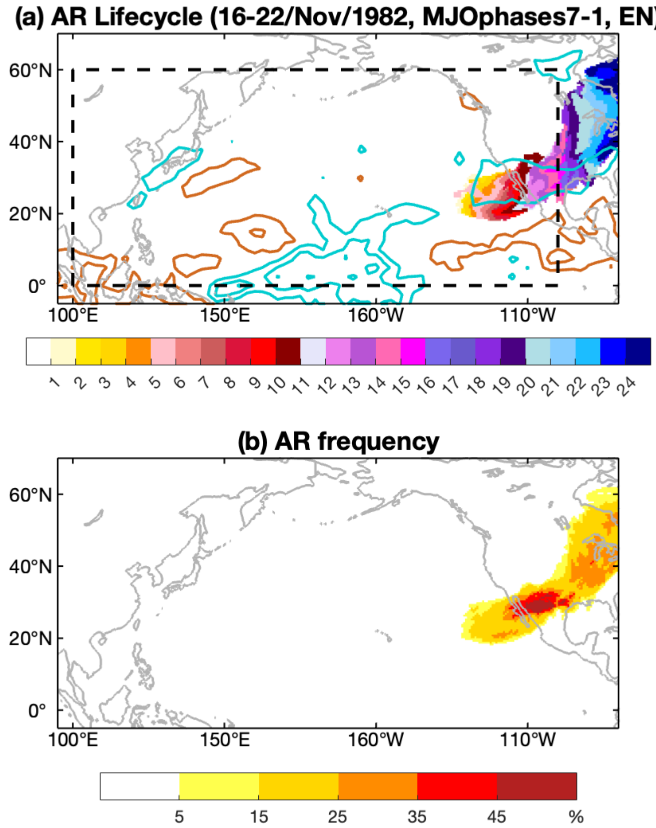

Fig. 1 Example of (a) AR lifecycle, and (b) AR frequency of a landfalling AR event during November 16-22, 1982 (in a similar fashion as Fig. 1 in Zhou, Kim and Waliser 2021). Dash box (0°N-60°N, 100°E-100°W) in (a) shows the focused region for AR lifecycles in this study. Shading in (a) represents the binary masks of AR objects in 6-hourly time steps starting from their origin (November 16 00Z). Brown/blue contours in (a) are 20-90-day filtered OLR anomalies for positive/negative values (20 Wm^{-2} interval, zero is omitted)

2.2.2 MJO phases

The MJO phases are defined according to the real-time multivariate MJO (RMM, Wheeler & Hendon 2004) index used to describe the MJO phase and amplitude. The RMM index consists of two principal components (RMM1 and RMM2) evaluated by the projection of the OLR and zonal winds at 850 and 200 hPa in the tropics onto the first combined empirical orthogonal function (EOF). When the amplitude ($A = [(\mathrm{RMM1})^2 + (\mathrm{RMM2})^2]^{\frac{1}{2}}$) of the MJO ≥ 1.0, the MJO is active. The eight MJO phases are determined by the 45° intervals from 0° to 360° of a phase angle $\theta = \tan^{-1}\left(\frac{RMM2}{RMM1}\right)$.

2.2.3 ENSO states

The ENSO states (EN, LN, and neutral) are classified (Table 1) according to the most prominent events obtained with the Oceanic Nino Index (ONI). EN years are listed when the ONI is equal to or greater than 0.8°C, and LN years are when the ONI is equal to or smaller than -0.8°C. Neutral is defined when the ONI is in between. The ONI index is based on the 3-month running mean of SST anomalies in the Niño 3.4 region (5°N-5°S, 170°W-120°W). Table 1 shows 11 EN, 12 LN, and 19 NT ENSO years.

Table 1: Dates of EN, LN, and neutral ENSO years obtained from the ONI index, considering the threshold of 0.8°C.

El Niño	1982/83, 1986/87, 1987/88, 1991/92, 1994/95, 1997/98, 2002/03, 2006/07, 2009/10, 2015/16, 2018/19
La Niña	1983/84, 1984/85, 1988/89, 1995/96, 1998/99, 1999/00, 2005/06, 2007/08, 2010/11, 2011/12, 2017/18
Neutral	1979/80, 1980/81, 1981/82, 1985/86, 1989/90, 1990/91, 1992/93, 1993/94, 1996/97, 2000/01, 2001/02, 2003/04, 2004/05, 2008/09, 2012/13, 2013/14, 2014/15, 2016/17, 2019/20

2.2.4 Composites for AR events under ENSO and MJO

Composites of AR frequency changes are made for each ENSO state (EN, LN, and neutral), each active MJO phase, and simultaneously under active EN and MJO phases 6-1. ARs must originate concurrently with the phase of ENSO and/or the MJO of interest, with the origin being within the dashed rectangle in Fig. 1a. The composites are constructed as follows: for example, for each active MJO phase, we compute the AR frequency with the selected AR events, and subtract the winter climatology (NDJFM). 66% of the total number of North Pacific AR events are selected when MJO is active. All composites are normalized by dividing by the winter AR frequency climatology to show the relative percentage changes.

From the 300 hPa daily wind data, we compute the zonally asymmetric streamfunction (Dawson 2016) and the mean zonal wind to assess the MJO tropical-extratropical teleconnection and the northern Pacific subtropical jet behavior, respectively, during AR events. The methods below describe how OLR, streamfunction, IVT, and precipitation composite anomalies are calculated for each active MJO phase. The daily climatological means are calculated by smoothing the daily means with a 31-day moving average, which acts as a filter to remove spurious variance due to the 41-year sample. The daily anomalies are obtained from the difference between the observed data on each day and the climatological mean for the same day. These anomalies are submitted to a bandpass Lanczos filter (Duchon 1979) with 211 weights, retaining only the intraseasonal variability in the 20-90 band. After this filtering, only the anomalies in NDJFM are used in the composites. The ENSO-related anomalies and the effect from other climate variability modes are removed from the composite anomalies since we are interested only in the EN effect on the MJO-AR connections.

The statistical significance of the composite anomalies is assessed with the Student's t-test (Wilks 2006). For the MJO filtered anomalies, the samples may exhibit serial dependence, characterized by the autocorrelation coefficient at lag 1, termed ρ_1. Hence, it is necessary to estimate the effective sample size $n = N\left(\frac{1-\rho_1}{1+\rho_1}\right)$, in which N is the original sample size (Wilks 2006).

2.2.5 Frequency of AR extreme precipitation events

We analyze the frequency of AR extreme precipitation events since they are related to potential natural disasters in North America, such as floods (Neiman et al. 2011) and landslides (Young, Skelly and Cordeira 2017). Extreme precipitation day identification at a given grid cell follows Grimm and Tedeschi (2009) by first computing the 3-day running mean of precipitation and fitting the running means to a gamma distribution. Days with precipitation amount exceeding the 90th percentile of the gamma distribution are considered extreme precipitation days. The probability of AR-linked extreme precipitation events is computed for the period between ARs making landfall and their termination over North America, considering ARs originated during an active phase of the MJO in all years and separately in EN years. This assumes that observed extreme rainfall during this time period is associated with an AR. We also calculate the climatological probability of AR-linked extreme precipitation events in NDJFM. The Student's t-test is applied to assess the significance of the difference between these MJO sample means (all years and EN years) and the climatology. Instead of showing this difference, we display the ratio between these probabilities to inform by which factor the probability changes in AR extreme events under the specific scenario (MJO in all years or MJO in EN years).

3 Climate modulation of North Pacific ARs

3.1 ENSO Modulation

Figure 2a shows the NDJFM climatological AR frequency. The AR activity intensifies over the North Pacific during this time period (Guan and Waliser 2015; Mundhenk, Barnes and Maloney 2016) with 98% of the total time steps over the 40 cool seasons associated with active ARs somewhere in the study domain. The maximum frequency extends from 160°E to 135°W over the subtropical northern Pacific where more than 12.5% of time steps have an AR.

The AR frequency is separated into EN and LN years (Fig. 2b-c) with composites of OLR, IVT, and circulation anomalies and mean zonal wind at 300 hPa shown in Fig. 2d-g. Figure S1 shows the same composites but in neutral ENSO years for comparisons with composites for EN and LN states. We assess the ENSO-AR connections since this information helps differentiate the straight effects of EN on ARs and the EN influence on the MJO-AR connections (next section). The EN teleconnection, which drives changes in AR activity over the northeastern Pacific (Patricola et al. 2020), is characterized by a cyclonic flow anomaly over the North Pacific, an anticyclonic flow anomaly over extratropical North America, and a secondary cyclonic flow in the southeastern US (Fig. 2f). LN teleconnection shows a nearly opposite circulation anomaly pattern (Fig. 2g).

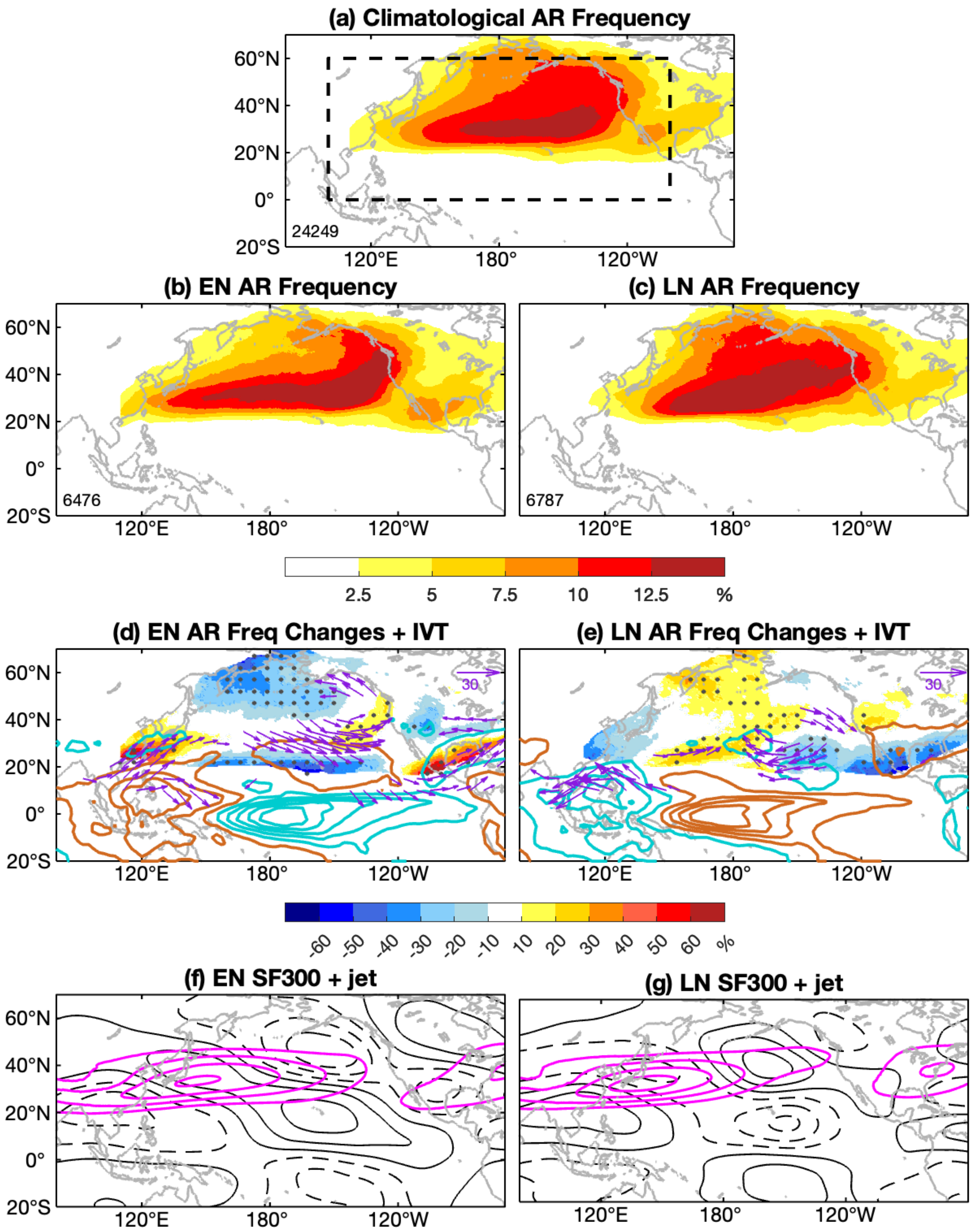

Fig. 2 (a) Winter (NDJFM) climatological AR frequency (percent of time steps) with North Pacific AR events originating in the black dash box (0°N-60°N, 100°E-100°W). Climatological AR frequency of North Pacific AR events in (b) EN, and (c) LN. Numbers written in (a), (b), and (c) are the time steps for all AR events in each sample. OLR anomalies (brown/blue contours for positive/negative values, $6\,Wm^{-2}$ interval, zero is omitted), IVT anomalies (purple arrows in units of $\mathrm{kg\,m^{-1}s^{-1}}$), and percentage changes in AR frequency (shading) in (d) EN and (e) LN. Dots mark AR frequency changes with $p < 0.1$ from a t-test. IVT anomalies are only shown to the north of 10°N and only for values over 15 $\mathrm{kg\,m^{-1}s^{-1}}$. 300 hPa streamfunction anomalies (continuous/dashed contours represent positive/negative values, $1.5\times10^{6}\,m^2s^{-1}$interval) and zonal wind (pink lines, 10 ms^{-1} interval, starting from 25 ms^{-1}) in (f) EN, and (g) LN. The zonal wind, IVT, OLR, and streamfunction anomalies are averaged between AR origins and terminations

EN (Fig. 2b) and LN (Fig. 2c) extend zonally the maximum frequency with respect to neutral (Fig. S1a). Overall, 27% (6476) of the total winter time steps (24249) related to North Pacific ARs happen in EN, 28% (6787) in LN, and 45% (10986) in neutral, but they are more frequent in neutral years because they are more numerous (19) than in EN (11), and LN (11) years (Table 1). On the other hand, the percentage of time steps with at least one AR somewhere over the North Pacific in each ENSO state in NDJFM is not different from climatology (98%) for the three ENSO states: 97% (EN), 98% (LN), and 98% (NT).

Under EN (Fig. 2d), a zonal band of strong anomalous eastward IVT and increased AR frequency appears between 20°N and 40°N over the North Pacific. AR frequency is increased by 10%-30% over the northeastern Pacific and west of the northwest US, associated with the deepened anomalous cyclonic flow. The eastward IVT anomaly aligns with the southern flank of the cyclonic circulation, and the southeastward extension of the northern Pacific subtropical jet (Fig. 2f). Previous studies have linked the Aleutian Low and the northern Pacific subtropical jet to enhanced zonal moisture transport in EN and increased AR activity over the northeastern Pacific (Kim, Zhou and Alexander 2017; Patricola et al. 2020). Increased AR origin frequency (20%-60% with respect to climatology) is found over eastern Asia, probably related to the northeastward IVT anomaly within the anticyclonic circulation linked to suppressed convection over the Maritime Continent and the western Pacific in EN (Fig. 2d). While AR origin frequency is not specifically plotted here, it is reasonable to assume that AR frequency reflects AR origins as this is a region with typically strong baroclinicity, and AR origins are more frequent toward the western boundaries of ocean basins (Guan and Waliser 2019). Increased AR frequency (by 20%-60%) is also present over Central America and the Caribbean Sea, corresponding to the anomalous northeastward IVT within the continental cyclonic flow anomaly (Fig. 2d,f).

AR frequency is suppressed by 10%-40% with respect to climatology over the extratropical western and central northern Pacific Basin in EN (Fig. 2d), associated with the westward IVT anomaly within the north branch of the intensified anomalous cyclonic circulation (Fig. 2d,f). Reduced AR frequency of a similar magnitude is also found over the southwestern US, corresponding to the westward IVT anomaly within the continental cyclonic flow.

Changes in AR frequency during LN (Fig. 2e) show nearly the opposite features from EN (Fig. 2d). AR frequency is reduced (10%-40% relative to climatology) over the subtropical northeastern Pacific, associated with the southwestward IVT anomaly within the anticyclonic flow (Fig. 2e,g). Suppressed frequency with a peak of 50% extends eastward into the Gulf of Mexico. AR origin frequency decreases by at least 30% over eastern Asia, probably related to the northwestward IVT anomaly within the anomalous cyclonic flow linked to enhanced convection over the Maritime Continent in LN (Fig. 2g).

Increased frequency by 10%-30% spreads between 20°N-60°N over the western and central northern Pacific in LN. The increase is associated with the convergence of anomalous northeastward IVT from the subtropical western Pacific and anomalous northwestward IVT within the North Pacific anticyclonic flow. The increased AR frequency reaches the northwest US (10%-30% relative to climatology), related to the northeastward extension of the northern Pacific subtropical jet (Fig. 2g) and the anomalous southeastward IVT at the northern flank of the anticyclonic flow (Fig. 2e).

Hence, changes in AR frequency under active ENSO over the northeastern Pacific are mainly affected by the ENSO teleconnection and the effect of ENSO on the subtropical jet (Payne and Magnusdottir 2014). Furthermore, these changes corroborate those shown by Mundhenk, Barnes and Maloney (2016) and Zhou et al. (2021), even though they apply other algorithms, constrain the cool-season as DJF, or consider an ENSO index (ENSO Longitude Index, ELI, Williams and Patricola 2018) that better correlates with the western US winter precipitation than other ENSO indices (Patricola et al. 2020). However, our results show EN and LN increasing AR activity over a wider area along the western North American coast, around 35°N-50°N. When the ENSO phenomenon is neutral the AR frequency (Fig. S1a) is similar to climatology (Fig. 2a). Changes in AR frequency in neutral ENSO (Fig. S1b) are weaker than those in active ENSO years compared to climatology (Fig 2d-e), as there is no ENSO teleconnection signal (Fig. S1c) over the North Pacific and the subtropical jet (Fig. S1c), OLR (Fig. S1b) and IVT (Fig. S1b) anomalies are weakened compared to those under EN (Fig. 2d,f) and LN (Fig. 2e,g).

3.2 MJO modulation

Figure 3 shows the evolution of AR frequency changes and associated IVT anomalies throughout the MJO cycle. MJO convection and tropical-extratropical teleconnections are also displayed. It is convenient to start the analysis from MJO phases 1-3 (Fig. 3a-c) when the suppressed MJO convection propagates over the Maritime Continent and reaches the western Pacific. Two anticyclonic anomalies straddle the equator at low-levels to the west of the suppressed convection (not shown), a typical Matsuno-Gill response (Gill 1980). The anomalous northeastward IVT within the anticyclonic flow south of Japan in MJO phases 2-3 (Fig. 3b-c) enhances AR origins up to 50% relative to climatology. The increased AR activity over eastern Asia extends eastwards towards the northwestern Pacific in MJO phase 3, probably related to the maximized northeastward IVT flux coupled with the enhanced MJO convection (Bretherton, Peters and Back 2004; Holloway and Neelin 2009; Zhou, Kim and Waliser 2021, Zhou et al. 2021).

Decreased AR frequency (20%-40%) emerges over the subtropical western Pacific in MJO phase 1 (Fig. 3a). In MJO phase 2 (Fig. 3b), these changes intensify (30%-50%) and shift to the subtropical central and northeastern Pacific, associated with the appearance of the MJO teleconnection and its anomalous anticyclonic flow and westward IVT. As the signal of the MJO teleconnection takes around 10-14 days to develop in the North Pacific (Seo and Lee 2017; Tseng, Maloney and Barnes 2019), the MJO teleconnection in an MJO phase (for example, MJO phase 3) is a composite for MJO teleconnections triggered in that MJO phase and also delayed signals from teleconnections originated in previous MJO phases (for example, MJO phase 2). In MJO phase 3 (Fig. 3c), decreased AR frequency over the subtropical central and northeastern Pacific peaks at 50%-70%, associated with the fully established MJO teleconnection, intensifying the anomalous anticyclonic flow (Stan et al. 2017) and westward IVT. AR frequency over North America decreases by 10%-50% over land between 30°N and 70°N in phases 2-3.

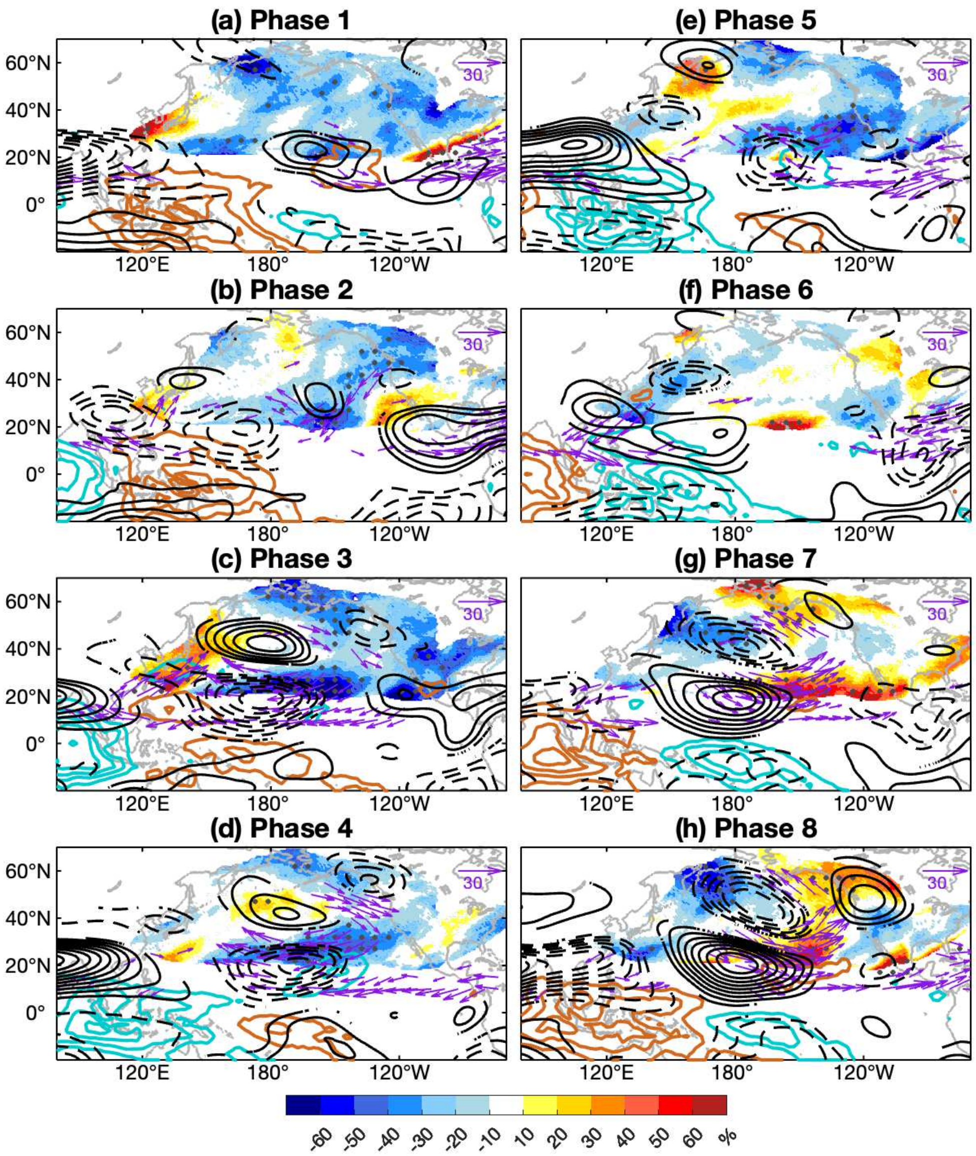

Fig. 3 Composites of percentage changes in AR frequency (shading), filtered 300 hPa streamfunction (continuous/dashed contours represent positive/negative values, $6 \times 10^5 m^2 s^{-1}$ interval, zero line is omitted), IVT (purple vectors, only showing values to the north of 10°N and over 15 $\mathrm{kg\,m^{-1}s^{-1}}$), and OLR (brown/blue contours represent positive/negative values, 5 W/m^2 interval, zero line is omitted) anomalies in each MJO phase. OLR anomalies are concurrent with AR origins. Streamfunction and IVT anomalies are averaged for dates when North Pacific ARs are active in each MJO phase. Dots, streamfunction contours, and IVT vectors represent AR frequency and MJO anomalies with p < 0.1 from a t-test

Reduced AR frequency persists over the northeastern Pacific in phase 4 (Fig. 3d), as the MJO teleconnection is still strong. In phase 5 (Fig. 3e), the suppressed MJO convection over the central Pacific weakens, and the MJO teleconnection decays, but the decreased AR frequency is still significant over the northeastern Pacific. Prevailing decreased AR frequency over the northeastern Pacific in MJO phases 2-5 was also shown by Mundhenk, Barnes and Maloney (2016), considering all seasons. Hence, changes in the AR frequency over this region are not symmetric with respect to their distribution throughout the MJO phases.

In MJO phases 5-7 (Fig. 3e-g), an opposite pattern in AR origin frequency emerges over the western Pacific when the enhanced MJO convection propagates over the Maritime Continent and reaches the western Pacific. Two cyclonic anomalies straddle the equator at low levels to the west of the enhanced convection (Fig. 1 of Gill 1980). The AR origin frequency decreases up to 50% over eastern Asia corresponding to the anomalous southwestward IVT within the cyclonic flow south of Japan in phases 6-7 (Fig. 3f-h). The decreased AR frequency over eastern Asia extends towards the northwestern Pacific and intensifies in phases 7 and 8, probably associated with the deepened North Pacific anomalous cyclonic flow.

Increased AR frequency intensifies and shifts to the subtropical central and northeastern Pacific in phase 6, associated with the appearance of the MJO tropical-extratropical teleconnection over the western Pacific, opposite to the pattern with respect to the teleconnection in phases 2-4 (Fig. 3b-d). Increased AR frequency (50%-70%) occurs over the subtropical northeastern Pacific in phase 7 (Fig. 3g) due to the intensification of the teleconnection pattern, the anomalous eastward IVT, and the cyclonic flow. These results are consistent with those associating increased AR activity with an intensified low over the northeastern Pacific (Stan et al. 2017) and enhanced MJO convection over the western Pacific (Guan et al. 2012; Guan and Waliser 2015; Payne and Magnusdottir 2014; Spry et al. 2014; Zhou, Kim and Waliser 2021, Zhou et al. 2021). In phase 8 (Fig. 3h), the MJO teleconnection pattern fully establishes between the North Pacific and North America. The increased AR frequency amplifies and extends northeastward, following the propagation of the cyclonic flow. Hence, the most prominent positive AR frequency changes over the northeastern Pacific happen in phases 7 and 8. In phase 1 (Fig. 3a), the MJO convection weakens over the central Pacific, the MJO teleconnection decays, and the increased AR activity quickly disappears over the northeastern Pacific.

4 EN influence on MJO-AR connections

Here we assess the joint impact from EN and MJO on North Pacific AR lifecycles. Figure 4 shows changes in the North Pacific AR activity and IVT anomalies from MJO phases 6 through 1 in all years (left panels, same as in Fig. 3) and EN years (right panels). MJO convection and teleconnections are also displayed. Note that the range in the color bar is larger in Fig. 4 than Fig. 3.

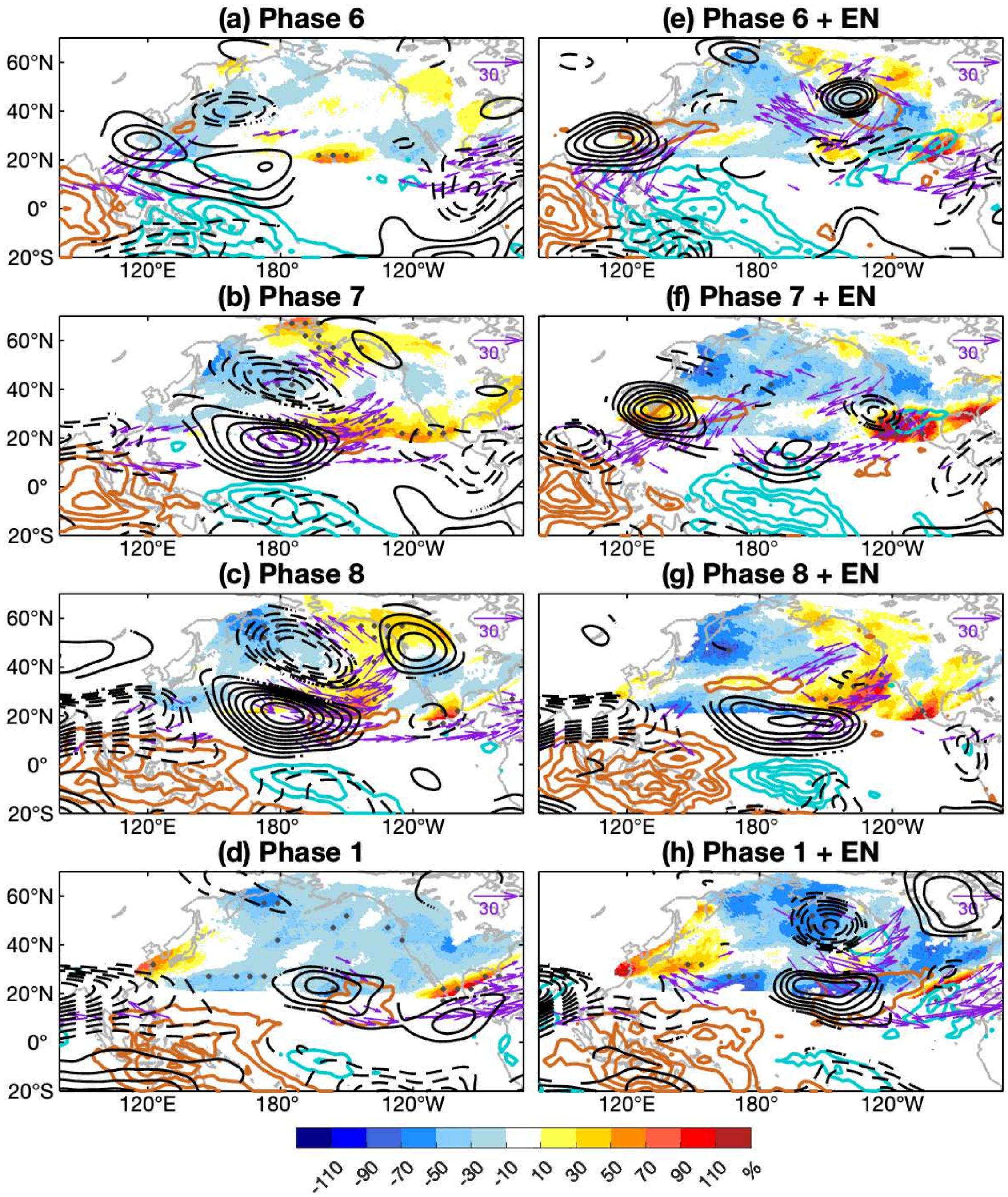

Fig. 4 Same as Figure 3, but the left panels show composites from MJO phase 6 through MJO phase 1 in all years, and the right panels show the same MJO phases in EN years

In MJO phase 6 (Fig. 4a), enhanced MJO convection propagates from the Maritime Continent and reaches the western Pacific. In EN (Fig. 4e), strong MJO equatorial convection (-10 W/m²) crosses 180° already in phase 6, favored by EN convection (Fig. 2d) due to ascent in the Walker circulation and positive SST anomalies. In composites for all years, this only occurs in phase 7 (Fig. 4b). Also, MJO convection over the western (phase 7) and central (phase 8) Pacific is enhanced (up to -20 W/m²) and shifted eastward in composites for EN (Fig. 4f-g) with respect to that for all years (Fig. 4b-c), consistent with previous studies showing an eastward shift of the MJO activity during EN events (Fink and Speth

1997; Hendon, Zhang and Glick 1999; Kessler 2001; Pohl and Matthews 2007; Tam and Lau 2005; Wei and Ren 2019).

The anomalous southwestward IVT within the anomalous cyclonic flow south of Japan and to the west of the MJO convection (Gill 1980) in phases 6-8 (Fig. 4a-c) is also stronger and shifted to the east in EN (Fig. 4e-g). Thus, origin frequency decreases over the western Pacific in phases 6-8 under EN (up to 70%, Fig. 4e-g) rather than over eastern Asia (Fig. 4a-c). AR origin frequency increases over eastern Asia in phases 7-8 and EN (MJO_{EN}phases7-8) (10%-50% with respect to climatology, Fig. 4f-g) corresponding to the anomalous northeastward IVT over eastern Asia and the western Pacific in EN (Fig. 2d). Also, the upper-level anomalous anticyclonic flow over eastern Asia and the western Pacific in MJO_{EN}phases6-7 is more persistent (Fig. 4e-f) because of the EN upper-level circulation anomalies with the same sign over this region (Fig. 2f).

Over the northeastern Pacific and western North America, changes in AR activity are maximized by the EN effect on MJO convection, propagation, and teleconnections. Increased AR frequency over the subtropical northeastern Pacific appears east of Hawaii in MJO_{EN}phases6-7 (Fig. 4e-f), potentially increasing the likelihood of “Pineapple Express” events. Moreover, maximum positive changes in AR frequency in MJO_{EN}phases6-8 surpasses 100%, extending from the northeastern Pacific towards California and Mexico (Fig. 4e-g) over regions not affected by the isolated effect of EN (Fig. 2d) or MJO (Fig. 4a-c). On the other hand, AR activity is increased by 110% over the southeastern US (Fig. 4f) associated with the superposition of MJO phase 7 (up to 50%, Fig. 4b) and EN (up to 60%, Fig. 2d) effects on North Pacific AR lifecycles.

The left panels in Fig. 5 display composites for the northern Pacific subtropical jet, AR activity, and MJO related-anomalies used as a reference for comparing MJO phases 7+8 in EN (Fig. 5a) and non-EN years (LN and neutral ENSO) (Fig. 5b) and the difference between them (Fig. 5c). As convection shifts to the east in EN, the MJO teleconnection is triggered east of 180° in MJO_{EN}phases7+8 (Fig. 5a). The teleconnection pattern weakens in MJO_{EN}phases7+8 with respect to that in non-EN years (Fig. 5b) and it propagates towards western subtropical North America (Fig. 5a) instead of elongating meridionally towards higher latitudes in the central northern Pacific (Fig. 5b). Results are consistent with the southeastward extension of the northern Pacific subtropical jet in EN (Fig. 5a, Fig. 2f) decreasing the Rossby wave propagation and reducing the MJO teleconnection pattern consistency (Tseng, Maloney and Barnes 2020). Composites from phases 6 through 1 in non-EN years are similar (not shown) to all years (Fig. 4, left panels) and show stronger MJO teleconnections than EN years, corroborating Tseng, Maloney and Barnes (2020) (Fig. 5b), even though they considered an MJO index based on convective variability (OMI index) instead of the RMM which is typically dominated by the wind field. Although the aspects described so far are visible in Figs. 4 and 5a-b, they are corroborated by the difference between EN and non-EN (Fig. 5c). It shows that the EN state predominantly increases the MJO-related convection anomalies in phases 7+8 in the central-eastern tropical Pacific and confirms the extension of the northern Pacific subtropical jet reaching the western North American coast, thus supporting the enhanced anomalous cyclonic flow and eastward IVT over that region.

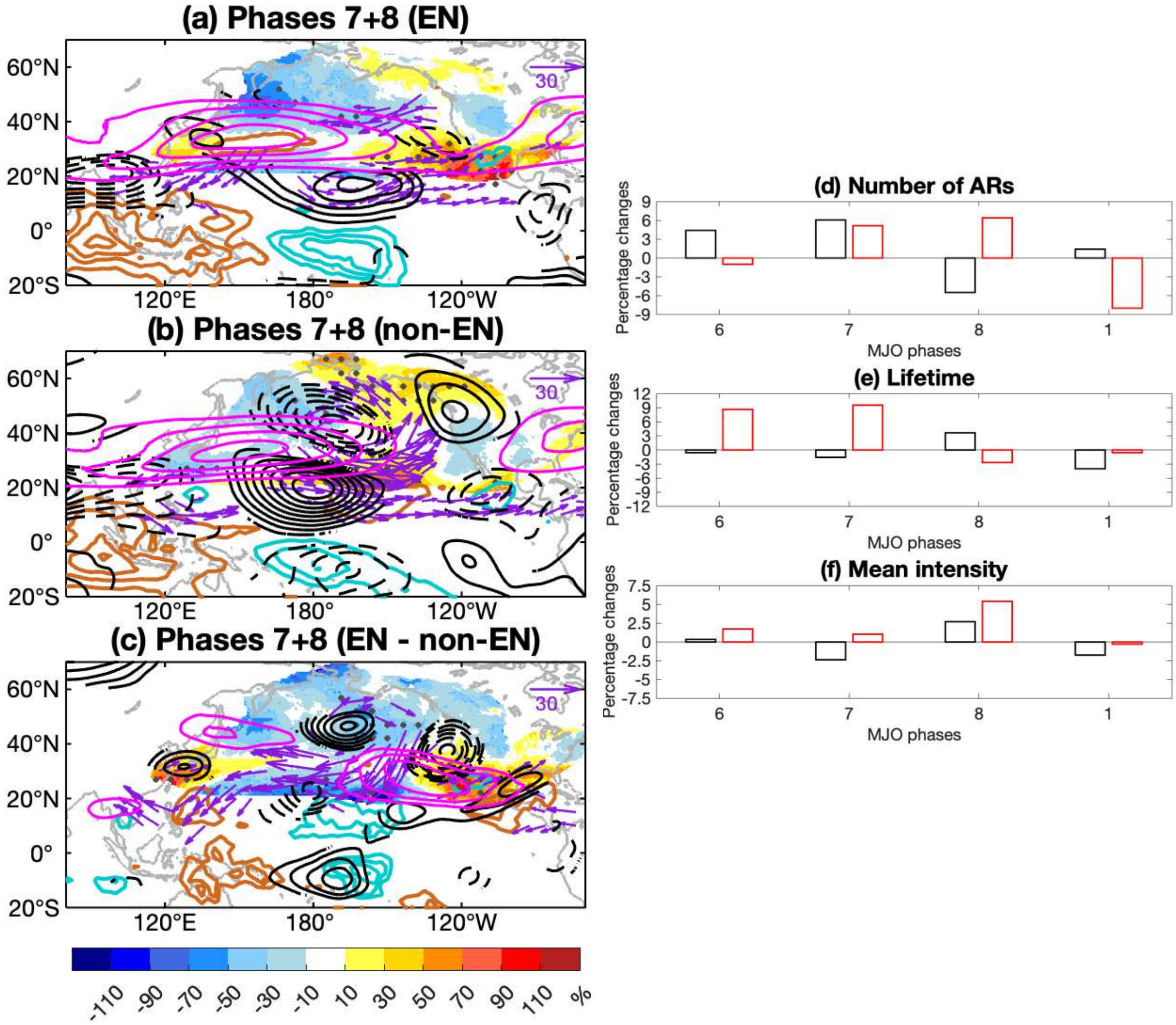

Fig. 5 Composites of percentage changes in AR frequency (shading), mean zonal wind (pink lines, 10 ms^{-1} interval, starting from 25 ms^{-1}), filtered 300 hPa streamfunction (continuous/dashed contours represent positive/negative values, $6 \times 10^5 m^2 s^{-1}$ interval, zero line is omitted), IVT (purple vectors, only showing values to the north of 10°N and over 15 $\mathrm{kg\,m^{-1}s^{-1}}$), and OLR (brown/blue contours represent positive/negative values, 5 W/m^2 interval, zero line is omitted) anomalies in MJO phases 7+8 in (a) EN and (b) and non-EN years. (c) The difference between (a) and (b). OLR anomalies are concurrent with AR origins. The mean zonal wind, streamfunction and IVT anomalies are averaged for dates when North Pacific ARs are active in each MJO phase. Dots, streamfunction contours, and IVT vectors represent AR frequency and MJO anomalies with $p < 0.1$ from a *t*-test. Percentage changes in (d) the number of AR events, (e) lifetime and (f) mean intensity over the North Pacific in MJO phases 6-1. Black bars show percentages for all years and red bars for EN years. NDJFM climatological values for number of AR events, lifetime, and mean intensity are 0.78 events/day, 2.72 days, and 388.52 $kg\,m^{-1}s^{-1}$, respectively

The right panels of Fig. 5 show the percentage changes in the number of AR events, lifetime, and mean intensity in MJO phases 6-1 for all years (black bars) and EN years (red bars). The increased number of AR events shifts from MJO phases 6-7 in all years to MJO phases 7-8 in EN years (Fig. 5d).

Furthermore, the number of AR events in MJO$_{EN}$phases7-8 increases by 5-6% in comparison with climatology (Fig. 5d), longer lifetimes happen in MJO$_{EN}$phases6-7 (Fig. 5e), and increased mean intensity in MJO$_{EN}$phases6-8 (Fig. 5f).

As the MJO convection and teleconnections in MJO$_{EN}$phases7+8 are shifted to the east (Fig. 5a), the upper-level cyclonic flow associated with increased AR activity and anomalous eastward IVT appears along the western North America coast rather than over the central northern Pacific (Fig. 5b). Although the anomalous cyclonic flow in EN is weakened (Fig. 4 right panels) with respect to composites for all years (Fig. 4 left panels), it lasts longer under EN, from MJO phases 6 through 1, because of the EN upper-level circulation anomalies with the same sign over the northeastern Pacific (Fig. 2f). These results are consistent with Moon, Wang and Ha (2011), which showed that in MJO phase 7, the North Pacific cyclonic flow is closer to the western US in EN, increasing precipitation over that region. Also, increased AR frequency reaches Alaska one phase earlier in EN (MJO phase 6, Fig. 4e) than in composites for all years (MJO phase 7, Fig. 4b) because the MJO teleconnection signal starts to appear over the northeastern Pacific earlier under the EN basic state.

Furthermore, MJO$_{EN}$phases6-1 (Fig. 4, right panels) show the upper-level anomalous cyclonic flow propagating along the western North American coast from subtropical through extratropical latitudes. In MJO$_{EN}$phases6-7, the cyclonic flow is centered around 25°N-30°N (Fig. 4e-f). Hence, maximum positive AR frequency is over subtropical North America in MJO$_{EN}$phase7. As the MJO propagates eastward slower under EN over the central-eastern tropical Pacific (Wei and Ren 2019), strong suppressed MJO convection reaches the subtropical northeastern Pacific earlier in all years (phase 8, Fig. 4c) than EN years (phase 1, Fig. 4h). Thus, the delayed MJO eastward propagation in EN allows the establishment of the anomalous IVT cyclonic flow over the subtropical northeastern Pacific shifted to the east in MJO$_{EN}$phases7-8 (Fig. 4f-g), with strong anomalous northeastward IVT coupled to the main MJO convection over the western and central Pacific.

The mechanisms behind these changes in AR lifecycle characteristics over the northeastern Pacific described thus far are complex since EN affects the basic state, the northern Pacific subtropical jet, the MJO convection, and its eastward propagation. Then, these changes influence the development and establishment of the MJO tropical-extratropical teleconnection and the anomalous eastward IVT flux related to North Pacific ARs.

The anomalous cyclonic flow propagates to higher latitudes in MJO$_{EN}$phase8 (Fig. 4g), surpassing 40°N in MJO$_{EN}$phase1 (Fig. 4h). Increased AR activity spreads over western North America in MJO$_{EN}$phase8, with positive changes over regions showing negative changes in composites for all years (Fig. 4c). Thus, the maximized impact on AR frequency over western North America occurs when the MJO convection and teleconnection (Fig. 3h) in phase 8 roughly align with the EN convection and teleconnection (Fig. 2d-f). Notwithstanding, the MJO teleconnection pattern strengthens and propagates towards extratropical latitudes in MJO$_{EN}$phase1 (Fig. 4h). The slow variation of the MJO probably favors delayed teleconnection signals in MJO$_{EN}$phase1 triggered by the enhanced MJO convection over the central Pacific in MJO$_{EN}$phase8 (Fig. 4g). The teleconnection pattern in MJO$_{EN}$phase1 supports the persistence of positive AR frequency over the northeastern Pacific and anomalous eastward IVT that point out towards the western US.

Figure 6 shows the frequency of MJO active days (Fig. 6a), AR origins over the North Pacific (Fig. 6b), and number of timesteps with landfalling ARs over North America (Fig. 6c) from MJO phase 6 through phase 1 in all years (black bars) and EN years (red bars). EN increases the climatological number of North Pacific AR events per day in NDJFM from 0.78 (Fig. 5) to 0.83, leading to an increased landfalling AR frequency over western North America (Payne and Magnusdottir 2014; Kim, Zhou and Alexander 2017). Furthermore, the total North Pacific AR events originating concurrently with active MJO phases also increases from 66% (subsection 2.2.4) to 73% in EN years. MJO phases 6 and 7 are more active than MJO phases 8 and 1 (Fig. 6a). Thus, North Pacific AR origins are more frequent in MJO phases 6 and 7 than MJO phases 8 and 1 (Fig. 6b). However, in EN, the frequency of MJO active days, and consequently, the number of AR origins decreases in MJO phases 6 and 7, and increases in phases 8 and 1 because the background EN-related anomalies influence the relative occurrence of MJO with similar patterns of circulation/convection anomalies (Fernandes and Grimm 2023). For example, MJO phases 8 and 1 are more frequent in EN because both modes in these phases support suppressed convection over the equatorial eastern Indian Ocean, Maritime Continent/western Pacific, while enhanced convection predominates over the equatorial central Pacific (Figs. 2d and 4c,d).

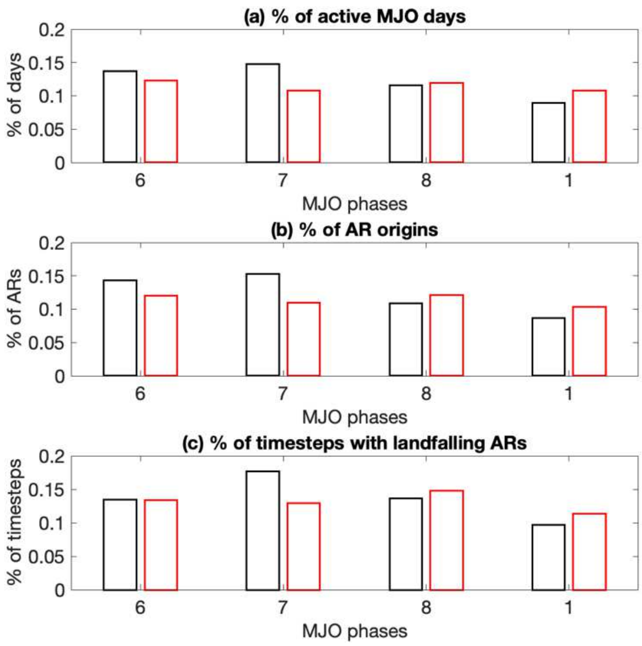

Fig. 6 Percentage of (a) MJO active days, (b) AR origins over the North Pacific (0°N-60°N, 100°E-100°W), and (c) timesteps with landfalling ARs over North America in MJO phases 6-1 in NDJFM. Black bars show percentages for all years and red bars for EN years

As an AR lifetime typically lasts longer than one MJO phase (~6-8 days) (see Fig. 1), ARs more often make landfall in North America from MJO phases 6 to 8, peaking in phase 7 (Fig. 6c). Results are consistent with those described in Mundhenk et al. (2018) and Zhou et al. (2021). Notwithstanding, in EN, ARs make landfall less often in phase 7 but more often in phases 8 and 1, with maximum frequency of landfalling happening later in phase 8. Changes in the peak of landfalling ARs over North America from phase 7 to phase 8 in EN are linked to the increased number of active MJO days in phase 8 (Fig. 6a) and also probably to the slower MJO propagation over the central-eastern tropical Pacific in EN (Wei and Ren 2019). Therefore, EN favors longer lifetimes to North Pacific AR events originated in MJO phases 6 and 7 (Fig. 5e) and also supports part of those events making landfall in North America later, in phases 8 and 1 (Fig. 6c). Composites for MJO-AR precipitation anomalies and extreme rainfall events during the landfalling ARs assessed here are in the next section.

5 EN influence on MJO-AR precipitation over North America

Here we assess how EN influences AR-related precipitation and extremes occurring from MJO phases 6 through 1 over North America. Precipitation statistics are only computed for dates in which an AR that originated in our study area has made landfall over North America and has not yet reached termination. In other words, precipitation is counted over North America only when an AR object is present over land. Composites are made using precipitation data from MERRA-2, although composites using CPC gridded rainfall show similar results over land (not shown). The significant positive precipitation anomalies are predominantly over the northeastern Pacific in all years (Fig. 7, left panels), with maximum anomalies happening in MJO phase 8 (Fig. 7c), corroborating Payne and Magnusdottir (2014), reaching the North American coast around 60°N, associated with increased AR activity over the same region in phases 7-8 (Fig. 4b-c).

An anomalous precipitation dipole occurs over the western North American coast from MJO_{EN}phase6 through MJO_{EN}phase8 (Fig. 7e-g), linked to the cyclonic flow anomaly adjacent to the continent (Fig. 4e-g). Positive precipitation anomalies are over coastal Alaska in MJO_{EN}phase6 (Fig. 7e) concurrent with the positive AR frequency changes and anomalous northeastward IVT (Fig. 4e). Negative precipitation anomalies appear over the western US in MJO_{EN}phase6 (Fig. 7e), related to the decreased AR frequency and anomalous southwestward IVT (Fig. 4e). Enhanced positive precipitation anomalies are also over the eastern US in MJO_{EN}phase6, associated with anomalous northeastward IVT and increased AR frequency linked to North Pacific ARs propagating from subtropical to extratropical continental regions (as in Fig. 1). These AR events are likely related to the significant variability in southeastern US rainfall under EN plus MJO phases 6+7 described by Arcodia, Kirtman and Siqueira (2020).

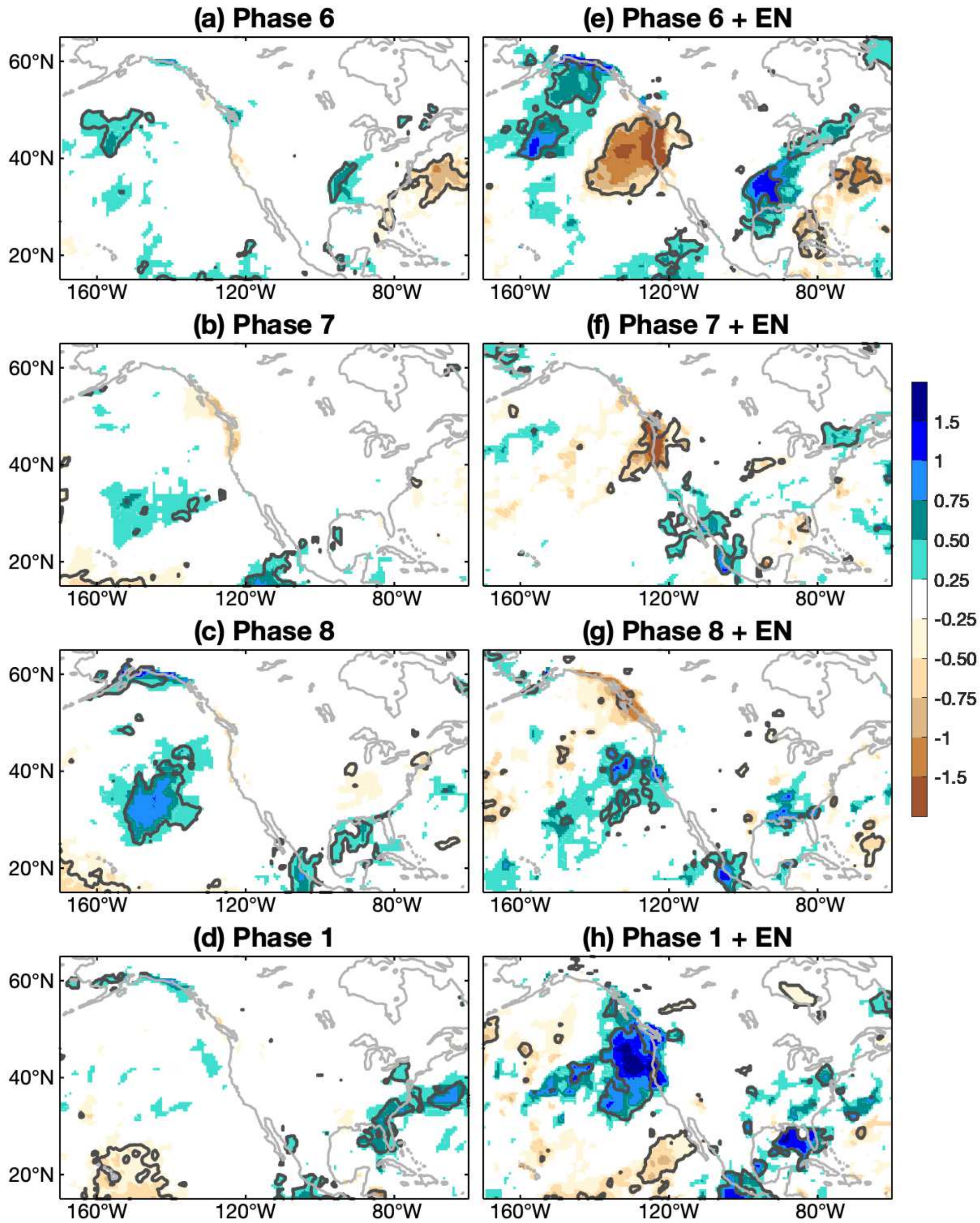

Fig. 7 Composites of precipitation anomalies (color bar, $mm\ day^{-1}$) in MJO phases 6-1 in all years (left panels) and in EN years (right panels). Precipitation anomalies are averaged for the dates between North Pacific ARs making landfall and their termination. Gray lines delimit values with $p < 0.1$ from a *t*-test

In MJO_{EN}phase7 (Fig. 7f), negative precipitation anomalies remain over the western US, and positive precipitation anomalies reach the subtropical western North America. Although the percentage of time steps with ARs making landfall over North America decreases in MJO_{EN}phase7 (Fig. 6c), positive precipitation anomalies are enhanced over the continent (Fig. 7f) with respect to those in all years (Fig. 7b). Notwithstanding, positive precipitation anomalies in MJO_{EN}phase6 (Fig. 7e) are stronger than those in MJO_{EN}phase7 (Fig. 7f), though positive changes in AR frequency increase in MJO_{EN}phase7 (Fig. 4f) with respect to MJO_{EN}phase6 (Fig. 4e). This is due to how we compute AR frequency (Figs. 3 and 4), namely for all ARs originating over the North Pacific, not only for those making landfall as in

Fig. 7. Hence, increased North Pacific AR activity does not necessarily mean increased precipitation anomalies over the North American due to landfalling ARs in the same MJO phase.

The anomalous precipitation dipole over western North America moves towards higher latitudes from MJO_{EN}phase7 (Fig. 7f) to MJO_{EN}phase8 (Fig. 7g), following the propagation of the anomalous cyclonic flow adjacent to western North America (Fig. 4f-g), with significant positive precipitation anomalies reaching the western US in MJO_{EN}phase8. Positive precipitation anomalies are shifted to the east (Fig. 7g) with respect to all years (Fig. 7c), following the displacement of MJO convection, teleconnection, and increased AR activity under EN (Fig. 4g). Notwithstanding, the maximum positive precipitation anomalies started in MJO_{EN}phase8 spread over coastal regions between 40°N and 55°N in MJO_{EN}phase1 (Fig. 7h), linked to the strengthened MJO tropical-extratropical teleconnection (Fig. 4h). Therefore, although the maximum AR frequency (Fig. 4g), mean intensity (Fig. 5c), and increased number of timesteps with ARs making landfall (Fig. 6c) are in MJO_{EN}phase8, the maximum positive precipitation anomalies last longer from MJO_{EN}phase8 to MJO_{EN}phase1. Positive precipitation anomalies over Mexico are also stronger in MJO_{EN}phases8-1 (Fig. 7g-h) because of the EN enhancement of cyclonic circulation (Fig. 2f) that favor precipitation in those regions.

Fig. 8 displays the ratio between the probability of AR extreme precipitation events for MJO phases 6-1 in all years (left panels) and EN years (right panels). The effect on the frequency of extremes (Fig. 8) follows that on daily precipitation (Fig. 7). However, there are instances when the impacts on the AR extreme precipitation are more prominent than in the AR average rainfall (Slinskey et al. 2020). For example, it happens in phases 6 and 8 over western Canada (Figs. 7a,c and 8a,c) and in phase 7 over southern California/Mexico (Figs. 7b and 8b). The most extensive MJO impacts on AR extreme rainfall events happen in phase 8 (Fig. 8c), in agreement with precipitation anomalies (Fig. 7c) and increased AR frequency (Fig. 4c). Changes in the frequency of AR extreme events weaken in phase 1 (Fig. 8d), as observed for the precipitation anomalies (Fig. 7d).

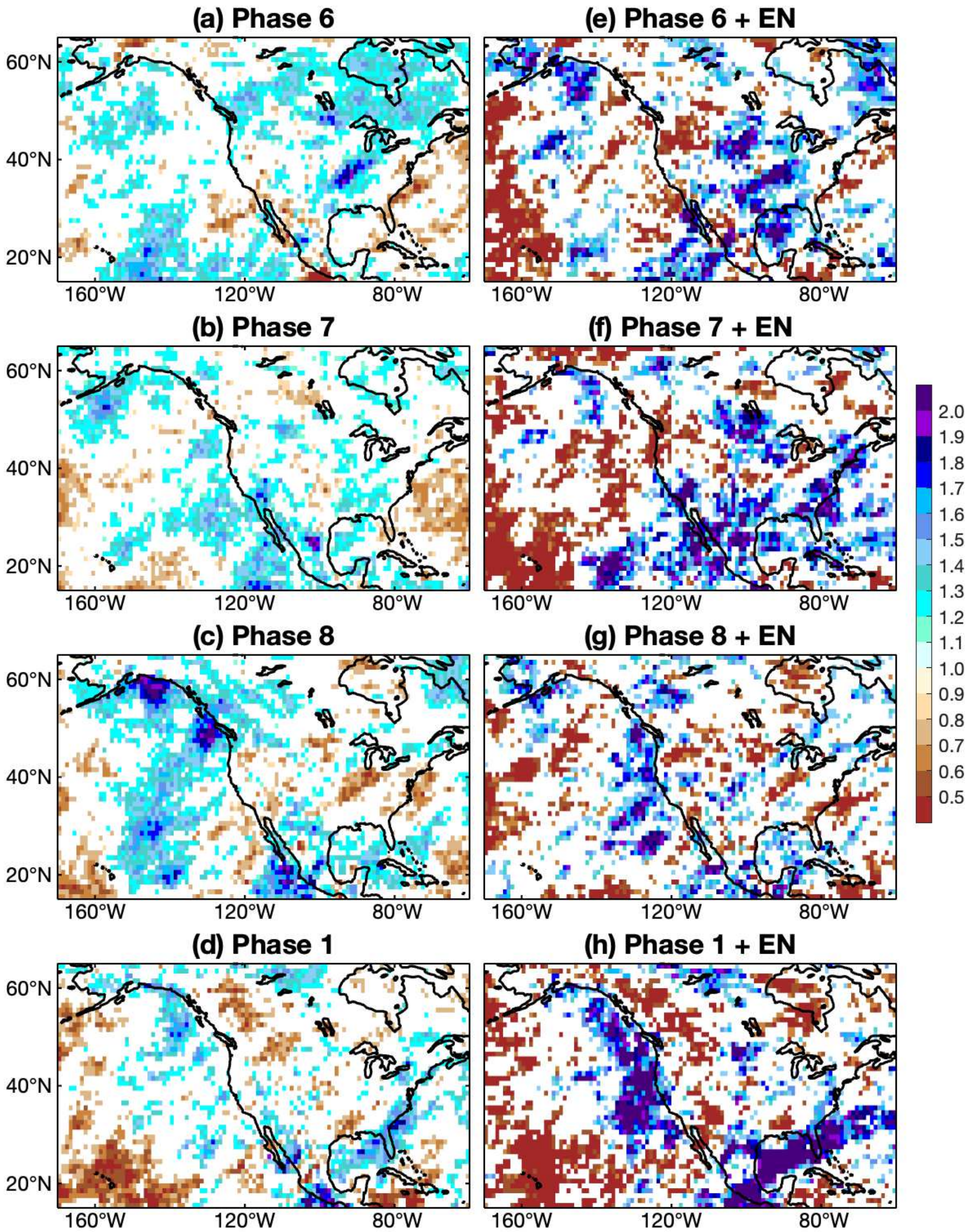

Fig. 8 Ratio between the probability of AR extreme precipitation events in MJO phases 6-1 and the mean probability (NDJFM), in (left) all years and (right) EN years. Only ratios corresponding to statistically significant difference between the probability of occurrence in MJO phases 6-1 and the mean probability with confidence level better than 90% are shown in color. When the proportion is larger than one, the frequency of MJO-AR extreme rainfall events increases by that factor under the specific scenario (all years or EN years). Extreme precipitation events are counted for the dates between North Pacific ARs making landfall and their termination

Changes in the frequency of extreme precipitation events follow the behavior of precipitation anomalies in MJO$_{EN}$phases6-1, showing increased significance over western North America (Fig. 8, right panels) associated with the anomalous cyclonic flow propagating closer to the continent (Fig. 4, right panels). Decreased frequency of extremes happens in MJO_{EN}phases6-7 over the western US (Fig. 8e-f), linked to negative precipitation anomalies (Fig. 7e-f) and decreased AR activity (Fig. 4e-f). Enhanced frequency of extreme events appears over Canada and Alaska in MJO_{EN}phase6 (Fig. 8e) in association with increased AR frequency and positive precipitation anomalies (Fig. 7e). Because of the eastward displacement of the MJO convection, teleconnection and AR activity, EN doubles the frequency of AR extreme precipitation events from subtropics in MJO phase 7 (Fig. 8f) through extratropical latitudes of western North America in MJO phases 8-1 (Fig. 8g-h). The most significant impacts happen one MJO phase later in EN (phase 1, Fig. 8c,h), following the EN effect on the enhanced precipitation anomalies (Fig. 7c,h). Furthermore, the EN enhancement of anomalous cyclonic circulation (Fig. 2f) over subtropical North America favors the increased frequency of AR extreme rainfall events (Fig. 8e-f) more than the AR positive precipitation anomalies (Fig. 7e-f) in MJO phases 6-7.

6 Summary and Discussion

This investigation addresses the EN influence on MJO-AR connections over the North Pacific and associated AR landfall-driven precipitation over North America from MJO phases 6 through 1. The background changes produced by EN modify the strength and position of the northern Pacific subtropical jet, the structure and propagation of the MJO's convection, as well as the associated MJO tropical-extratropical teleconnection (Fink and Speth 1997; Moon, Wang and Ha 2011) affecting MJO-AR connections over the North Pacific and their lifecycle characteristics (Figs. 4, 5 and 6). MJO convection over the western (phase 7, Fig. 4f) and central (phase 8, Fig. 4g) Pacific is shifted eastward and is enhanced in EN, influencing the development of the MJO teleconnection pattern associated with North Pacific ARs. The MJO teleconnection is triggered east of 180° in MJO_{EN}phases7+8, propagating towards western subtropical North America (Fig. 5a). In MJO_{EN}phase1, the MJO teleconnection strengthens as it propagates towards extratropical North America (Fig. 4h), probably related to delayed MJO teleconnection signals triggered from the enhanced MJO convection in MJO_{EN}phase8 (Fig. 4g). As the MJO convection and teleconnection shift to the east, the upper-level cyclonic flow associated with increased AR activity appears along the western North American coast, persisting until MJO_{EN}phase1. Maximum AR frequency increases in MJO_{EN}phase6-8 and is shifted to the east (Fig. 4e-g), over regions not influenced by the isolated effect of EN and MJO (Fig. 4a-c). Although the teleconnection pattern weakens in MJO_{EN}phase7-8 (Tseng, Maloney and Barnes 2020), the slower MJO eastward propagation in MJO_{EN}phases6-8 (Wei and Ren 2019) allows the anomalous IVT cyclonic flow to be established over the subtropical northeastern Pacific, with a northeastward IVT component coupled to the enhanced MJO convection over the western (MJO_{EN}phase7, Fig. 4f) and central (MJO_{EN}phase8, Fig. 4g) Pacific, supporting increased AR activity.

Moreover, the EN background increases the number of North Pacific AR events per day, their lifetime, and mean intensity from MJO phases 6 through 8 (Fig. 5d-f), the number of MJO active days and AR origins in phases 8-1, besides delaying the peak of ARs making landfall over North America from phase 7 to phase 8 (Fig. 6). Hence, positive precipitation anomalies (Fig. 7) and increased frequency of extreme rainfall events (Fig. 8) related to landfalling ARs over western North America are more to the east and also peak later, lasting from MJO_{EN}phase8 to MJO_{EN}phase1. The main conclusions explained above are meaningful since they have potential to improve subseasonal predictions of North Pacific ARs when EN and MJO are active. Results may also provide a reference for evaluating the ability of subseasonal to seasonal models to simulate MJO-AR rainfall over North America under the EN state and yield a process-based diagnosis for model biases.

The conclusions described here are based on the Guan and Waliser (2019) approach, which has shown improved detection/tracking sensitivity (Guan and Waliser 2019) with respect to older tracking algorithms (Sellars et al. 2017; Zhou, Kim and Guan 2018). Also, although ENSO-AR connections over the North Pacific agree with findings from previous studies (Mundhenk, Barnes and Maloney 2016; Kim, Zhou and Alexander 2017; Patricola et al. 2020; Zhou et al. 2021), the strongest MJO-AR connections corroborate those shown by Payne and Magnusdottir (2014), Guan and Waliser (2015) and Mundhenk, Barnes and Maloney (2016) but differ of those in Zhou, Kim and Waliser (2021) and Zhou et al. (2021). Even if results show here display similar features observed in Zhou, Kim and Waliser (2021) and Zhou et al. (2021), for example, changes in AR origin frequency over eastern Asia associated with a Gill-type response to MJO forcing (Gill 1980; Bao and Hartmann 2014), and the propagation of ARs aligned with the circulation of the MJO teleconnection, the most significant MJO impacts on AR activity over the northeastern Pacific shift one MJO phase later (3-4, 7-8), a topic which deserves further investigation.

Additional ongoing research is focused on whether the LN background (Fig. 2e,g), which favors MJO tropical-extratropical teleconnections in MJO phases 3-4 (Tseng, Maloney and Barnes 2020), may support more ARs making landfall and impacting the extratropical North American rainfall in these MJO phases through increased AR activity and anomalous eastward IVT over the northern flank of the North Pacific anticyclonic flow (Fig. 3c-d).

Acknowledgments Support for this work was provided by the National Aeronautics and Space Administration (NASA) Modeling Analysis and Prediction Program. We gratefully acknowledge the availability of the output from the Guan and Waliser (2019) algorithm, which makes this work possible. We thank Bin Guan for his assistance in the tracking algorithm dataset.

References

Arcodia MC, Kirtman BP, Siqueira LSP (2020) How MJO teleconnections and ENSO interference impacts U.S. precipitation. J Clim 33:4621–4640. https://doi.org/10.1175/JCLI-D-19-0448.1

Baggett CF et al (2017) Advancing atmospheric river forecasts into subseasonal-to-seasonal time scales. Geophys Res Lett 44:7528–7536. https://doi.org/10.1002/2017GL074434

Bao M, Hartmann DL (2014) The response to MJO-like forcing in a nonlinear shallow-water model. Geophys Res Lett 41:1322–1328. https://doi.org/10.1002/2013GL057683

Bjerknes J (1969) Atmospheric teleconnections from the equatorial Pacific. Mon Wea Rev 97:163–172. https://doi.org/10.1175/1520-0493(1969)097<0163:ATFTEP>2.3.CO;2

Bozkurt D et al (2021) Influence of African Atmospheric Rivers on Precipitation and Snowmelt in the Near East's Highlands. J Geophys Res: Atmos 126. https://doi.org/10.1029/2020JD033646

Bretherton CS, Peters ME, Back LE (2004) Relationships between water vapor path and Precipitation over the Tropical Oceans. J Clim 17: 1517–1528. https://doi.org/10.1175/1520-0442(2004)017<1517:RBWVPA>2.0.CO;2

Chakraborty S et al (2021) Extending the Atmospheric River concept to Aerosols: Climate and Air Quality Impacts. Geophys Res Lett 48. https://doi.org/10.1029/2020GL091827

Chen M et al (2008) Assessing objective techniques for gauge-based analyses of global daily precipitation. J Geophys Res 113. https://doi.org/10.1029/2007JD009132

Dawson A (2016) Windspharm: A High-Level Library for Global Wind Field Computations Using Spherical Harmonics. J Open Res Software 4. https://doi.org/10.5334/jors.129

DeFlorio MJ et al (2018) Global evaluation of atmospheric river subseasonal prediction skill. Clim Dyn 52:3039–3060. https://doi.org/10.1007/s00382-018-4309-x

DeFlorio MJ et al (2019) Experimental Subseasonal-to-Seasonal (S2S) Forecasting of Atmospheric Rivers Over the Western United States. J Geophys Res: Atmos 124:11242–11265. https://doi.org/10.1029/2019JD031200

Dettinger MD et al (2011) Atmospheric rivers, floods and the water resources of California. Water (Switzerland) 3:445–478. https://doi.org/10.3390/w3020445

Dominguez F et al (2018) Tracking an atmospheric river in a warmer climate: From water vapor to economic impacts. Earth System Dyn 9:249–266. https://doi.org/10.5194/esd-9-249-2018

Duchon CE (1979) Lanczos Filtering in One and Two Dimensions. J Appl Meteor 18:1016–1022. https://doi.org/10.1175/1520-0450(1979)018<1016:LFIOAT>2.0.CO;2

Fernandes LG, Grimm AM (2023) Global ENSO modulation of MJO and its impacts on South America. J Clim. https://doi.org/10.1175/JCLI-D-22-0781.1

Fink A, Speth P (1997) Some potential forcing mechanisms of the year-to-year variability of the tropical convection and its intraseasonal (25-70-day) variability. Int J Climatol 17:1513–1534. https://doi.org/10.1002/(SICI)1097-0088(19971130)17:14<1513::AID-JOC210>3.0.CO;2-U

Gelaro R et al (2017) The modern-era retrospective analysis for research and applications, version 2 (MERRA-2). J Clim 30:5419–5454. https://doi.org/10.1175/JCLI-D-16-0758.1

Gill AE (1980) Some simple solutions for heat-induced tropical circulation. Quart J R Met Soc 106:447–462. https://doi.org/10.1002/qj.49710644905

Grimm AM, Tedeschi RG (2009) ENSO and extreme rainfall events in South America. J Clim 22:1589–1609. https://doi.org/10.1175/2008JCLI2429.1

Guan B et al (2012) Does the Madden-Julian oscillation influence wintertime atmospheric rivers and snowpack in the sierra nevada? Mon Weather Rev 140:325–342. https://doi.org/10.1175/MWR-D-11-00087.1

Guan B et al (2013) The 2010/2011 snow season in California's Sierra Nevada: Role of atmospheric rivers and modes of large-scale variability. Water Resources Res 49:6731–6743. https://doi.org/10.1002/wrcr.20537

Guan B, Waliser DE (2015) Detection of atmospheric rivers: Evaluation and application of an algorithm for global studies. J Geophys Res 120:12,514-12,535. https://doi.org/10.1002/2015JD024257

Guan B, Waliser DE (2019) Tracking Atmospheric Rivers Globally: Spatial Distributions and Temporal Evolution of Life Cycle Characteristics. J Geophys Res: Atmos 124:12523–12552. https://doi.org/10.1029/2019JD031205

Guan B, Waliser DE, Martin Ralph F (2018) An intercomparison between reanalysis and dropsonde observations of the total water vapor transport in individual atmospheric rivers. J Hydrometeor 19:321–337. https://doi.org/10.1175/JHM-D-17-0114.1

Guan B, Waliser DE, Martin Ralph F (2023) Global Application of the Atmospheric River Scale. J Geophys Res: Atmos 128. https://doi.org/10.1029/2022JD037180

Hendon HH, Zhang C, Glick JD (1999) Interannual Variation of the Madden-Julian Oscillation during Austral Summer. J Clim 12:2538–2550. https://doi.org/10.1175/1520-0442(1999)012<2538:ivotmj>2.0.co;2

Holloway CE, Neelin DJ (2009) Moisture vertical structure, column water vapor, and tropical deep convection. J Atmos Science 66:1665–1683. https://doi.org/10.1175/2008JAS2806.1

Kessler WS (2001) EOF Representations of the Madden-Julian Oscillation and Its Connection with ENSO. J Clim 14:3055–3061. https://doi.org/10.1175/1520-0442(2001)014<3055:EROTMJ>2.0.CO;2

Kim H-M, Zhou Y, Alexander MA (2017) Changes in atmospheric rivers and moisture transport over the Northeast Pacific and western North America in response to ENSO diversity. Clim Dyn 52:7375–7388. https://doi.org/10.1007/s00382-017-3598-9

Kim S, Chiang JCH (2021) Atmospheric river lifecycle characteristics shaped by synoptic conditions at genesis. Int J Clim 42:521–538. https://doi.org/10.1002/joc.7258

Lee S, Polvani LM and Guan B (2022) Modulation of Atmospheric Rivers by the Arctic Stratospheric Polar Vortex. Geophys Res Lett 49. https://doi.org/10.1029/2022GL100381

Leung LR, Qian Y (2009) Atmospheric rivers induced heavy precipitation and flooding in the western US simulated by the WRF regional climate model. Geophys Res Lett 36. https://doi.org/10.1029/2008GL036445

Liebmann B, Smith CA (1996) Description of a Complete (Interpolated) Outgoing Longwave Radiation Dataset. Bull Am Meteor Soc 77:1275-1277. https://www.jstor.org/stable/26233278

Moon JY, Wang B, Ha K (2011) ENSO regulation of MJO teleconnection. Clim Dyn 37:1133–1149. https://doi.org/10.1007/s00382-010-0902-3

Mundhenk BD, Barnes EA, Maloney ED (2016) All-season climatology and variability of atmospheric river frequencies over the North Pacific. J Clim 29:4885–4903. https://doi.org/10.1175/JCLI-D-15-0655.1

Mundhenk BD et al (2018) Skillful empirical subseasonal prediction of landfalling atmospheric river activity using the Madden–Julian oscillation and quasi-biennial oscillation. npj Clim Atmos Science 1. https://doi.org/10.1038/s41612-017-0008-2

Nash D et al (2022) Winter and spring atmospheric rivers in High Mountain Asia: climatology, dynamics, and variability. Clim Dyn 58:2309–2331. https://doi.org/10.1007/s00382-021-06008-z

Neiman PJ et al (2008a) Diagnosis of an intense atmospheric river impacting the pacific northwest: Storm summary and offshore vertical structure observed with COSMIC satellite retrievals. Mon Wea Rev 136:4398–4420. https://doi.org/10.1175/2008MWR2550.1

Neiman PJ et al (2008b) Meteorological characteristics and overland precipitation impacts of atmospheric rivers affecting the West coast of North America based on eight years of SSM/I satellite observations. J Hydrometeor 9:22–47. https://doi.org/10.1175/2007JHM855.1

Neiman, PJ et al (2011) Flooding in Western Washington: The Connection to Atmospheric Rivers. J Hydrometeor 12: 1337–1358. https://doi.org/10.1175/2011JHM1358.1

Patricola CM et al (2020) Maximizing ENSO as a source of western US hydroclimate predictability. Clim Dyn 54:351–372. https://doi.org/10.1007/s00382-019-05004-8

Payne AE, Magnusdottir G (2014) Dynamics of landfalling atmospheric rivers over the North Pacific in 30 years of MERRA reanalysis. J Clim 27:7133–7150. https://doi.org/10.1175/JCLI-D-14-00034.1

Prince HD et al (2021) Genesis Locations of the Costliest Atmospheric Rivers Impacting the Western United States. Geophys Res Lett 48. https://doi.org/10.1029/2021GL093947

Pohl B, Matthews AJ (2007) Observed Changes in the Lifetime and Amplitude of the Madden-Julian Oscillation Associated with Interannual ENSO Sea Surface Temperature Anomalies. J Clim 20:2659–2674. https://doi.org/10.1175/JCLI4230.1

Ralph FM et al (2006) Flooding on California's Russian River: Role of atmospheric rivers. Geophys Res Lett 33(13). https://doi.org/10.1029/2006GL026689

Ralph FM et al (2019) A Scale to Characterize the Strength and Impacts of Atmospheric Rivers. Bull A Meteor Soc 100:269–289. https://doi.org/10.1175/BAMS-D-18-0023.1

Roundy PE et al (2010) Modulation of the Global Atmospheric Circulation by Combined Activity in the Madden-Julian Oscillation and the El Niño-Southern Oscillation during Boreal Winter. J Clim 23:4045–4059. https://doi.org/10.1175/2010JCLI3446.1

Sellars SL et al (2017) Genesis, Pathways, and Terminations of Intense Global Water Vapor Transport in Association with Large-Scale Climate Patterns. Geophys Res Lett, 44:12,465-12,475. https://doi.org/10.1002/2017GL075495

Seo K-H, Lee H-J (2017) Mechanisms for a PNA-like tele- connection pattern in response to the MJO. J. Atmos. Sci. 74:1767–1781. https://doi.org/10.1175/JAS-D-16-0343.1

Shearer EJ et al (2020) Examination of Global Midlatitude Atmospheric River Lifecycles Using an Object-Oriented Methodology. J Geophys Res: Atmos 125(22). https://doi.org/10.1029/2020JD033425

Slinskey EA et al (2020) A Climatology of Atmospheric Rivers and Associated Precipitation for the Seven U.S. National Climate Assessment Regions. J Hydrometeor 21: 2439–2456 https://doi.org/10.1175/JHM-D-20

Spry CM et al (2014) Characterizing Pineapple Express storms in the Lower Mainland of British Columbia, Canada. Canadian Water Res J 39:302–323. https://doi.org/10.1080/07011784.2014.942574

Stan C et al (2017) Review of Tropical-Extratropical Teleconnections on Intraseasonal Time Scales. Rev Geophys 55:902–937. https://doi.org/10.1002/2016RG000538

Tam CY, Lau NC (2005) Modulation of the Madden-Julian Oscillation by ENSO: Inferences from observations and GCM simulations. J Meteorol Soc Jpn 83:727–743. https://doi.org/10.2151/jmsj.83.727

Toride K et al (2019) Model-based probable maximum precipitation estimation: How to estimate the worst-case scenario induced by atmospheric rivers? J Hydrometeor 20:2383–2400. https://doi.org/10.1175/JHM-D-19-0039.1

Toride K, Hakim G (2021) Influence of Low-Frequency PNA Variability on MJO Teleconnections to North American Atmospheric River Activity. Geophys Res Lett 48(13). https://doi.org/10.1029/2021GL094078

Tseng KC, Maloney E, Barnes EA (2019) The consistency of MJO teleconnection patterns: An explanation using linear Rossby wave theory. J. Clim 32:531–548. https://doi.org/10.1175/ JCLI-D-18-0211.1.

Tseng KC, Maloney E, Barnes EA (2020) The consistency of MJO teleconnection patterns on interannual time scales. J Clim 33:3471–3486. https://doi.org/10.1175/JCLI-D-19-0510.1

Warner MD, Mass CF, Salatheé EP (2012) Wintertime extreme precipitation events along the Pacific Northwest Coast: Climatology and synoptic evolution. Mon Wea Rev 140:2021–2043. https://doi.org/10.1175/MWR-D-11-00197.1

Vitart F, Robertson AW, S2S Steering Group (2015) Sub-seasonal to seasonal prediction: Linking weather and climate. Seamless Prediction of the Earth System: From Minutes to Months, G. Brunet, S. Jones, and P. M. Ruti, Eds., WMO-1156, World Meteorological Organization, 385–401. http://library.wmo.int/pmb_ged/wmo_1156_en.pdf.

Wei Y, Ren HL (2019) Modulation of ENSO on fast and slow MJO modes during boreal winter. J Clim 32:7483–7506. https://doi.org/10.1175/JCLI-D-19-0013.1

Wheeler MC, Hendon HH (2004) An All-Season Real-Time Multivariate MJO Index: Development of an Index for Monitoring and Prediction. Mon Weather Rev 132:1917–1932. https://doi.org/10.1175/1520-0493(2004)132<1917:AARMMI>2.0.CO;2

Wilks DS (2006) Statistical methods in the atmospheric sciences. Academic Press, London

Williams IN, Patricola CM (2018) Diversity of ENSO events unified by convective threshold sea surface temperature: A nonlinear ENSO index. Geophys Res Lett 45: 9236–9244. https://doi.org/10.1029/2018gl079203

Young AM, Skelly KT, Cordeira JM (2017) High-impact hydrologic events and atmospheric rivers in California: An investigation using the NCEI Storm Events Database. Geophys Res Lett 44:3393–3401. https://doi.org/10.1002/2017GL073077

Zhang C (2005) The Madden-Julian Oscillation. Rev Geophys 43:RG2003

Zhou Y, Kim H, Guan B (2018) Life Cycle of Atmospheric Rivers: Identification and Climatological Characteristics. J Geophys Res: Atmos 123:12,715–12,725. https://doi.org/10.1029/2018JD029180

Zhou Y et al (2021) Uncertainties in Atmospheric River Lifecycles by Detection Algorithm: Climatology and Variability. J Geophys Res: Atmos 126. https://doi.org/10.1029/2020JD033711

Zhou Y, Kim H, Waliser DE (2021) Atmospheric River Lifecycle Responses to the Madden-Julian Oscillation. Geophys Res Lett 48. https://doi.org/10.1029/2020GL090983

Zhu Y, Newell RE (1994) Atmospheric Rivers and Bombs. Geophys Res Lett 21. https://doi.org/10.1029/94GL01710

Zhu Y, Newell RE (1998) A Proposed Algorithm for Moisture Fluxes from Atmospheric Rivers. Mon Wea Rev 126: 725–735. https://doi.org/10.1175/1520-0493(1998)126<0725:APAFMF>2.0.CO;2

Declarations

Funding:
This work was funded by the National Aeronautics and Space Administration (NASA) Modeling Analysis and Prediction Program (MAP) # 80NSSC21K1501

Conflicts of interest/Competing interests:
There are no conflicts of interest.

Availability of data and material:
The data used in this research are available at the websites of the institutions cited in the text.

Code availability:
Not applicable.

Authors' contributions:
L.G.F. performed data procurement and processing, methods development, and analysis and wrote the first draft of the manuscript. P.C.L. provided project support and contributions to methods, results, and manuscript writing.

Supplementary Files

This is a list of supplementary files associated with this preprint. Click to download.

- Supplementarymaterial.docx